PHYSICS

X-ray phase measurements by time-energy correlated photon pairs

Yishai Klein[1,2,3]*, Edward Strizhevsky[1,3], Haim Aknin[1,3], Moshe Deutsch[1], Eliahu Cohen[4], Avi Pe'er[1], Kenji Tamasaku[3], Tobias Schulli[5], Ebrahim Karimi[2,6], Sharon Shwartz[1,3]

The resolution of a measurement system is fundamentally constrained by the wavelength of the used wave packet and the numerical aperture of the optical system. Overcoming these limits requires advanced interferometric techniques exploiting quantum correlations. While quantum interferometry can surpass the Heisenberg limit, it has been confined to the optical domain. Extending it to x-rays enables sub-angstrom spatial and zeptosecond temporal resolution, unlocking atomic-scale processes inaccessible to existing methods. Here, we demonstrate x-ray quantum interferometry using 17.5–kilo–electron volt ($\lambda = 70$ picometers) photon pairs. Our approach introduces a phase measurement technique with exceptional noise resilience, mitigating the impact of mechanical instabilities, vibrations, and photonic noise—key challenges in x-ray interferometry. By generating and using entangled x-ray photons, we lay the foundation for next-generation techniques with unprecedented phase precision. This breakthrough carries far-reaching consequences for fundamental physics, high-resolution imaging, and spectroscopy, bringing to light quantum optical effects never before accessed in the x-ray regime.

INTRODUCTION

Interferometers are the most direct and sensitive instruments for phase measurements, playing a pivotal role in fundamental science and numerous applications. The demand for higher performance has driven the development of advanced interferometers, sparking great interest across a broad range of disciplines. The conventional approach to phase sensing with interferometers relies on amplitude-splitting a beam into two, each of which follows a different spatial path, and a subsequent recombination of these beams. Constructive or destructive interference occurs depending on the relative phase between the two waves. Thus, the detected intensity provides information on the relative phase between the waves.

This approach was adapted to x-rays by Bonse and Hart (*1*), who replaced standard beam splitters and mirrors, used in the optical regime, by reflecting lattice planes in devices cut from perfect silicon crystals. As shown in Fig. 1A, such an interferometer uses three crystal lamellae. The first splits the beam into two (transmitted and Laue-reflected), and the second Laue reflects and recombines them to create an interference pattern on the third lamella, used to detect intensity variations in the interference pattern when a phase object is inserted into one of the interfering beams. This lamella uses its angstrom-scale atomic structure periodicity to detect the intensity variation in the interference pattern on the angstrom-scale, dictated, in turn, by the x-rays' angstrom-scale wavelength.

The invention of x-ray interferometers has led to advanced phase-sensing devices that are invaluable in various applications. These include the precise measurement of universal constants, e.g., the Avogadro number (*2*, *3*), of lattice parameters of perfect crystals (*4*, *5*), and phase-contrast imaging, which resolves details that standard absorption imaging cannot capture (*6*–*9*). However, the sensitivity and robustness of conventional x-ray interferometers are highly susceptible to vibration and fabrication imprecisions due to the short wavelength (*10*, *11*). Monolithic crystal x-ray interferometers provide higher immunity to vibrations and mechanical noise but impose limits on imaged object size and fabrication tolerances (*10*, *11*). Perfect crystal x-ray interferometers also mandate the use of highly monochromatic input beams that are extremely sensitive to various types of scattering and stray radiation, which can severely degrade the quality of the information they provide. While other types of x-ray interferometers based on diffraction and propagation (*8*, *9*, *12*, *13*) have demonstrated advantages in certain aspects, their phase sensitivity is limited compared to crystal-based x-ray interferometers (*10*, *11*). Notably, all existing x-ray interferometers rely on beam or single-photon interference without any correlation between the photons. Introducing quantum correlations could enhance their sensitivity and immunity to noise, unlocking new possibilities for precision measurements and ultrafast time-resolved studies.

Here, we present an alternative approach to x-ray interferometry that exploits quantum correlations and coincidence measurements between photon pairs. Building on the foundations of quantum interferometry (*14*) and recent advances in quantum-enhanced protocols, we implement the SU(1,1) interferometer scheme (*15*, *16*). This scheme is intrinsically broadband and supports large acceptance angles, properties that make it exceptionally well-suited for x-ray spontaneous parametric down-conversion (SPDC), used here to generate strongly correlated photon pairs. The result is a system that offers two major capabilities: It enables phase-contrast imaging at the nanoscale and provides a pathway to interferometric access of ultrafast temporal dynamics—regimes that remain inaccessible to classical x-ray techniques.

While coincidence-based methods at high photon energies have previously been applied in radioactive decay studies, including for interferometric effects (*17*–*19*), and quantum correlations have recently been used for x-ray imaging (*20*, *21*), our work demonstrates quantum interference in the generation of highly correlated x-ray

[1]Physics Department and Institute of Nanotechnology and Advanced Materials, Bar-Ilan University, Ramat Gan 52900, Israel. [2]Nexus for Quantum Technologies, University of Ottawa, Ottawa, Ontario K1N 6N5, Canada. [3]RIKEN SPring-8 Center, 1-1-1 Kouto, Sayo-cho, Sayo-gun, Hyogo 679-5148, Japan. [4]Faculty of Engineering and Institute of Nanotechnology and Advanced Materials, Bar-Ilan University, Ramat Gan 52900, Israel. [5]ESRF–The European Synchrotron, Grenoble 38043, France. [6]Institute for Quantum Studies, Chapman University, Orange, CA 92866, USA.
*Corresponding author. Email: yishaykl@gmail.com

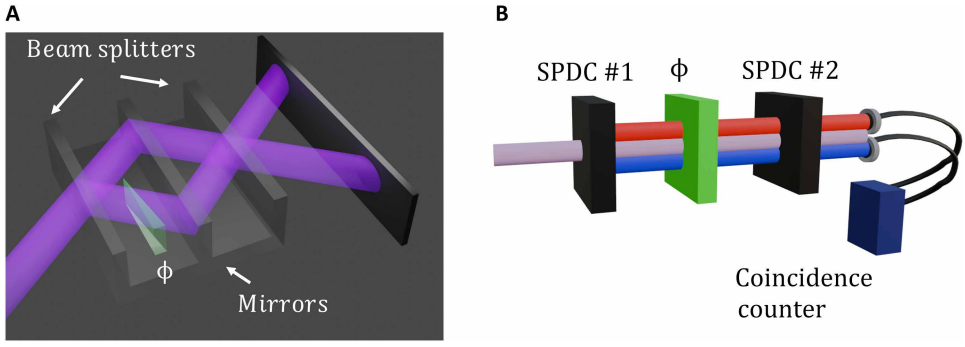

Fig. 1. Comparison of Mach-Zehnder and SU(1,1) Interferometers. (**A**) X-ray Mach-Zehnder interferometer: Laue diffraction in the leftmost lamella of a monolithic crystal interferometer generates two beams that are Laue reflected by the second lamella to interfere at the position of the third lamella, causing the resultant intensities to vary depending on the relative phase difference between the two waves. (**B**) SU(1,1) interferometer: Nonlinear crystals replace the beam splitters. These generate from the pump beam (purple) by parametric down-conversion two photons: idler (blue) and signal (red) detected by two detectors with coincidence discrimination. The intensity at the output (detectors) depends on the interference between the modes. A phase object placed between the two crystals introduces different phase shifts due to wavelength dispersion, yielding a corresponding change in the counted intensity. This allows for the detection of relative phase shifts by intensity measurements.

photon pairs. This interference not only confirms the coherence of the SPDC source but also leads to a notable enhancement in the signal-to-noise ratio (SNR) of phase measurements. In doing so, it establishes a foundation for a new class of quantum-enabled x-ray metrology.

The SU(1,1) interferometer and other quantum interferometers have been widely implemented in the optical regime (*15*, *16*, *22*–*27*) but never with x-rays and offer several marked advantages over other types of interferometers. These advantages include robustness against vibrations (*22*), ability to use parametric gain to improve SNR (*25*), reduced sample dose (*26*), and capability to overcome system losses and inefficient detection (*24*, *26*, *28*, *29*).

The operating principle of the SU(1,1) interferometer (*15*, *16*, *22*), which relies on the phase dependence of nonlinear optical mixers and amplifiers, is illustrated in Fig. 1B. When two nonlinear media are arranged sequentially to generate photon pairs, e.g., through SPDC, the phase difference becomes measurable through the detection of the photons emerging from the second crystal. Specifically, the flow of energy in the second crystal, from the pump to SPDC or vice versa, depends on the relative phase between the SPDC photon pairs and the pump ($\Delta\phi = \phi_s + \phi_i - \phi_p$). Quantum mechanically, the process is a biphoton interference mechanism, where photons can be generated or annihilated only in pairs, which leads to nonclassical squeezing and is key to the utilization of SU(1,1) interference in quantum applications of sensing, communication, computing, etc. (*30*, *31*). Introducing an object between the two crystals causes considerable phase accumulation differences between the pump, signal, and idler beams due to dispersion, resulting, in turn, in a change in the photon count rate of the signal and idler. Varying this phase shift by varying, e.g., the object's thickness, results in intensity variations in the counters akin to interference patterns. The count rate variation enables, therefore, an accurate determination of the phase shift variation.

Crucially, in the x-ray regime, the refractive index deviates from unity by only 10^{-5} to 10^{-6}, a seemingly small difference with profound consequences. Specifically, the change in the membrane's refractive index between the pump and the down-converted photons (signal and idler) can exceed the refractive index contrast between the membrane and air. Consequently, the dispersion-induced phase accumulates nearly twice as rapidly as in standard x-ray interferometers. This effect highlights another intrinsic advantage of the SU(1,1) configuration—its enhanced sensitivity to spectral phase—further distinguishing it from conventional interferometric schemes.

RESULTS

Setup and procedure

The design is based on the key principles demonstrated in the SU(1,1) interferometers at optical wavelengths, with necessary modifications for x-rays (*20*, *21*, *32*) as depicted in Fig. 2A and described below. The two major differences between x-ray and conventional SPDCs are the nonlinear mechanism and the phase matching scheme. Here, the nonlinearity is based on a plasma-like nonlinearity (*33*–*35*), and the phase matching is based on the atomic-scale periodicity of crystals (*36*) as shown in Fig. 2B. Both the nonlinearity and the phase matching scheme impose a geometry where the signal and idler beams propagate at angles nearly twice the Bragg angle with respect to the pump beam (*36*). To mitigate the absorption effect and facilitate small angular shifts between the photons for optimizing the beams' overlap, we used a high energy, 35 keV, for the pump. Since ensuring beam overlap is crucial for SU(1,1) interferometers, we use a monolithic silicon crystal (*37*, *38*) with two lamellae spaced 5 mm apart. As the Laue-reflecting planes in both lamellae are perfectly aligned in a monolithic crystal device, the need for separate relative alignments of two crystals is eliminated. A monolithic crystal device is also a perfect solution to the challenges associated with beam overlap. To satisfy phase matching, the interferometer was tuned to an angle of 55.85 mrad, deviating from the Bragg angle by 0.15 mrad. The phase objects inserted between the device's lamellae were silicon membrane combinations of varying thicknesses ranging from 2 to 28 μm (see the Materials and Methods for more details about the interferometer and phase objects).

One of the major advantages of quantum sensing is its capability to use multiple correlations across various degrees of freedom of the emerging photons to enhance the SNR of the measured signal (*21*, *39*, *40*). In this work, we primarily focus on time, energy, and propagation angle. To demonstrate this, we recorded both the time

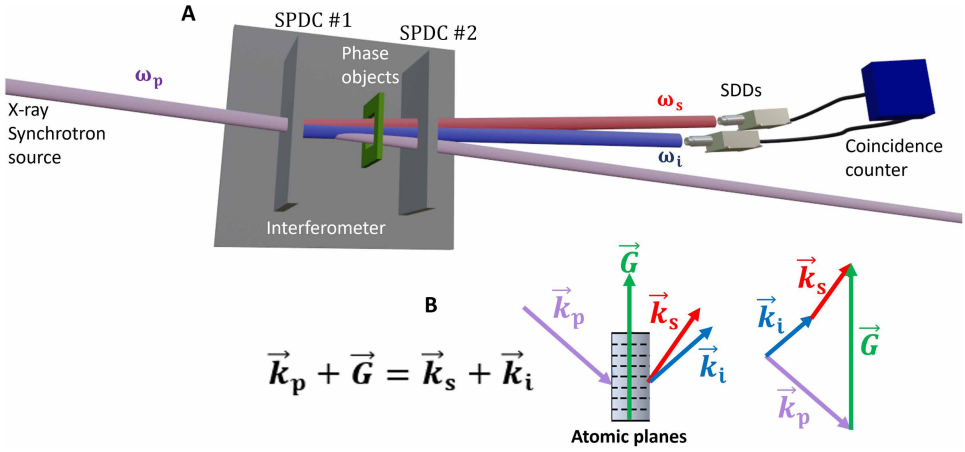

Fig. 2. Experimental scheme of the x-ray SU(1,1) interferometer. (**A**) A 35-keV beam enters the interferometer, constructed from a monolithic silicon crystal with two lamellae. The coincidence count rate at the detectors varies depending on the phase shift caused by a phase object inserted between the lamellae. (**B**) X-ray SPDC phase matching diagram where $\vec{k}_p$, $\vec{k}_s$, and $\vec{k}_i$ are, respectively, the wave vectors of the pump, signal, and idler, and $\vec{G}$ is the lattice vector.

and the energy of each detected photon (by a resolution that far exceeds the uncertainly limit), then postselected photon pairs (detected at phase-matching angles) complying with energy conservation, and analyzed the temporal distribution of their time difference. This suggested that coincidence measurements could improve the SNR by a factor inversely proportional to the biphoton correlation time, which could be as small as 100 zs for x-rays. However, practical enhancement of the SNR is limited by the response time of the detectors, which is several orders of magnitude larger than the envelope of the biphoton states. Despite this inherent limitation, leveraging the temporal distribution can effectively contribute to the reduction of background noise, as we now show.

Figure 3 demonstrates the impact of energy and temporal filtering. The average raw spectrum measured in one detector is shown in Fig. 3A. The low-energy range below 7 keV is dominated by fluorescence and detector noise, while the count rates observed above 21 keV primarily result from Compton scattering within the sample and surrounding materials. The energy-filtered data, obtained using the photon energy resolving capabilities of our detectors to select photons in the center range of 14 to 21 keV, is shown in blue. Note that this is not the full range of the SPDC, but the range that optimizes the SNR for our specific setup.

Despite the initial energy filtering, a substantial level of background noise remains within our region of interest. This residual noise originates primarily from the Compton tail, as well as fluorescence from materials along the beam path, such as lead and iron shielding, and from components within the detector itself, including copper and nickel. To further reduce the background, we used a fast coincidence scheme, implemented via a high-speed digitizer that captured the detector signals within a 1000-ns coincidence window. The resulting time-difference histogram, shown in Fig. 3B, reveals a peak at zero time delay, indicating the presence of coincident events. However, the signal remains obscured by the background, making it challenging to unambiguously identify photon pairs.

To further enhance the SNR, we exploit the fact that the sum of the energies of the generated photons must equal the energy of the pump photon, in accordance with energy conservation. The results after applying this constraint are shown in Fig. 3C, which presents a Gaussian distribution on top of a nearly constant background. Next, to isolate the Gaussian distribution associated with the SPDC photons, we subtract the average of the two outermost bins that represent the uniform background distribution to better observe the Gaussian distribution of the SPDC photons (Fig. 3D). For comparison, Fig. 3E shows the counts that do not satisfy energy conservation. A Gaussian fit to the data in Fig. 3D yields a detector response time of ~200 ns. This background subtraction procedure enables the detection of subtle phase variations, even in the presence of much stronger noise.

Observations

Following the procedure described above, we conducted a series of coincidence measurements with the silicon membrane phase objects, of thicknesses varying from 0 to 28 μm, inserted into the beam path. The key results of this study are displayed in Fig. 4A as green symbols, accompanied by corresponding error bars. The red line in Fig. 4A represents the theoretically calculated curve, which will be discussed in the next section. As shown, there is a clear agreement between the experimental data and the theoretical prediction.

To further support our results, Fig. 4B shows unfiltered data, which primarily consist of accidental coincidence counts (black diamonds) recorded without applying energy conservation filtering or subtracting the uniform background associated with the temporal filter. For comparison, the same theoretical curve shown in Fig. 4A (red line) is overlaid on the unfiltered data. As expected, no phase-dependent modulation is observed in the unfiltered data. Moreover, repeated measurements using the same 24-μm-thick membrane yield inconsistent background noise. In contrast, the corresponding filtered data points are so consistent that they appear visually indistinguishable. This clearly indicates that the modulation seen in Fig. 4A cannot be attributed to accidental coincidences.

To reinforce this conclusion and quantify the quantum enhancement, we fitted both the filtered and the unfiltered datasets to a cosine-squared function predicted by the theoretical model. We evaluated the fit quality using the coefficient of determination, defined as $R^2 = 1 - \frac{\sum (y_i - f_i)^2}{\sum (y_i - \bar{y})^2}$ where y_i are the measured data points, f_i are the corresponding values of the fitted function, and $\bar{y}$ is the mean of the measured data. The filtered data yield a high R^2 value of

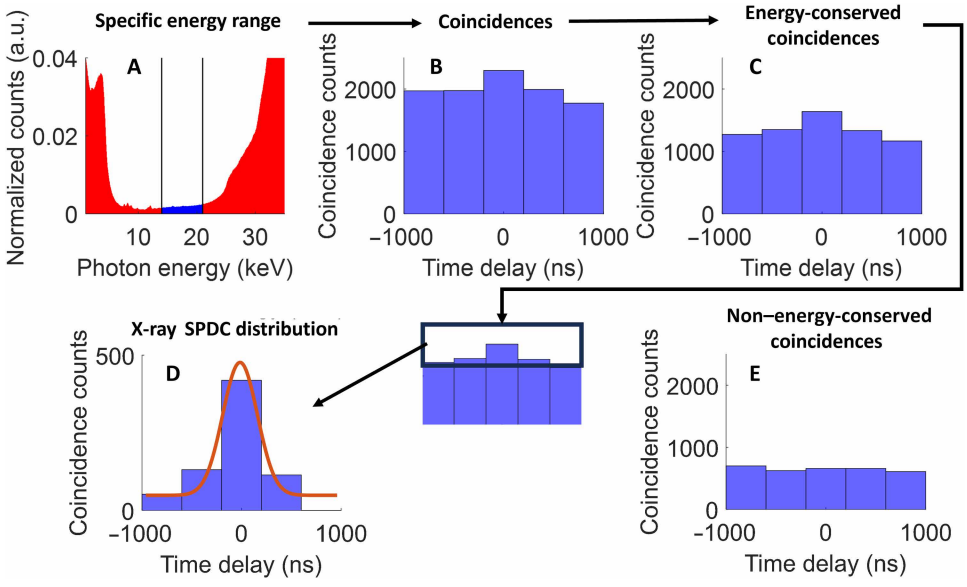

Fig. 3. The process of noise filtering. (**A**) Full spectrum as measured by a single detector. The blue shadow indicates the energy range selected for SNR optimization. (**B** to **E**) Time difference histograms: (B) with time coincidence but without energy conservation discrimination; (C) same as (B) but with energy conservation discrimination; (D) the data in (C) after the subtraction of the constant baseline spanned by the two outermost bins in (C). This baseline is generated by accidental coincidences, which are independent of the time difference. The red curve is a Gaussian fit yielding the actual temporal resolution of our system: 200-ns half width at half maximum. (E) Counts that do not conserve energy exhibit a nearly uniform distribution, confirming random arrival times of background photon pairs. a.u., arbitrary units.

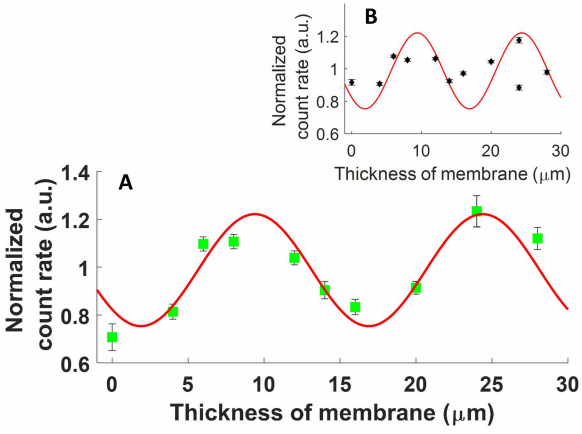

Fig. 4. Experimental results. Normalized coincidence count rate at the output of the second lamella dependence on the thickness of the membranes. (**A**) Measured SPDC count rate after using temporal and energy filtering (green squares) and theoretical curve (red line). The measurement time for each point was ~6 hours. Two separate measurements were performed on the 24-μm membrane at different times; both points are plotted but cannot be distinguished at this scale. (**B**) Count rate without applying energy or temporal filtering (black diamonds), under the same normalized theoretical model used in (A) (red line). In both figures, each dataset was normalized by its average count rate

0.9, consistent with the predicted periodicity from the simulation. But in the unfiltered case, the R^2 drops to just 0.3, which is low enough that you could fit the data to other periodic function and get a similar result. In other words, there is no real correlation with the physics. It is just noise.

The relatively large fluctuations observed in the unfiltered data likely stem from our use of Kapton tape to secure the membrane without adhesive. For each measurement, the membrane (and thus the Kapton) was removed and reinserted, not always at the same position on the tape. Because of manufacturing tolerances, this introduced slight variations in the effective Kapton thickness at the beam location—on the order of a few hundred nanometers. While the dispersion of Kapton can be considered approximately flat at this scale, variations in thickness and surface roughness can lead to differences in scattering. Our measurements of the interference fringes are robust against such scattering effects; however, the unfiltered background noise may be influenced by these variations. Despite these fluctuations, the extracted phase remained stable, further underscoring the resilience of our measurement technique.

It is worth noting that even in the filtered data, the agreement with the theoretical prediction is not perfect, and small deviations are evident—some of which exceed the expected shot noise. These discrepancies could be attributed to fluctuations in the pump power or to minor changes in the phase-matching angle, which was realigned for each data point.

Comparison with theory

To calculate the coincidence count rate, we used the Glauber correlation function

$$G^{(2)}(\tau,\mu)=\left\langle a_{si}^{\dagger}(t_2,\mathbf{r_2})a_{id}^{\dagger}(t_1,\mathbf{r_1})a_{id}(t_1,\mathbf{r_1})a_{si}(t_2,\mathbf{r_2})\right\rangle \quad (1)$$

at the output of the second lamella. Here, a_{si} and a_{id} are signal and idler annihilation operators, respectively, $\mu=\mathbf{r_2}-\mathbf{r_1}$, and $\tau=t_2-t_1$. The count rates were obtained by numerically integrating Eq. 1 over the spectral and angular bandwidths. The operators are calculated in the frequency domain by considering the propagation through the three elements (the two lamellae and the phase object), including the loss and Langevin operators. This approach ensures the

preservation of the commutators. The x-ray SPDC process was computed by solving the coupled wave equations for the signal and idler (*34*) in each of the lamellae

$$\begin{aligned}\frac{\partial a_{si}}{\partial z}+\frac{\alpha_{si}}{\cos(\theta_{si})}a_{si}&=\kappa a_{id}^{\dagger}e^{i\Delta kz}+\sqrt{\frac{2\alpha_{si}}{\cos(\alpha_{si})}}f_{si}\\ \frac{\partial a_{id}^{\dagger}}{\partial z}+\frac{\alpha_{id}}{\cos(\theta_{id})}a_{si}^{\dagger}&=-\kappa^{*}a_{si}e^{i\Delta kz}+\sqrt{\frac{2\alpha_{id}}{\cos(\alpha_{id})}}f_{id}^{\dagger}\end{aligned}\tag{2}$$

Here, θ_{si} and θ_{id} are the signal and idler angles; α_{si} and α_{id} are the absorption coefficients at the signal and idler frequencies, respectively, f_{si} and f_{id} are the Langevin noise operators, and κ is the nonlinear coupling coefficient. The phase of the object placed between the lamellae was represented by $e^{i\Delta\phi}$ where the phase shift $\Delta\phi$ is given by (*22*)

$$\begin{aligned}\Delta\phi&=\phi_{si}+\phi_{id}-\phi_{p}\\&=2\pi d\left(\frac{n_{si}}{\lambda_{si}}+\frac{n_{id}}{\lambda_{id}}-\frac{n_{p}}{\lambda_{p}}\right)\end{aligned}\tag{3}$$

where λ_p, λ_{si}, λ_{id}, n_p, n_{si}, n_{id}, and d are, respectively, the wavelengths, the silicon membrane's indices of refraction for the pump, signal, and idler, and the thickness of the membranes. For further mathematical details, see Supplementary Text.

The experimental results shown in Fig. 4 are in good agreement with the normalized simulated curve. This agreement required three adjustments of the theoretical curve: a vertical shift, a count rate scaling, and a horizontal shift. These correspond, respectively, to a nonperfect overlap between the beams, uncertainties in the pump flux, and a possible phase shift between the signal and idler and the pump even when no phase object is present in the space between the lamellae. The scaling is consistent with a pump flux of around 10^{12} photons per second, in good agreement with the flux of the synchrotron beam. The comparison between the experiment results and the theory indicates that the phase shift in the absence of the membranes is $\sim\pi/3$ corresponding to the gap between the two lamellae. The required vertical shift was 0.043 counts per second. The simulated visibility is 0.93, assuming an ideal beams overlap, whereas in our experiment, we observed a visibility of approximately 0.27 (as reflected in the vertical shift we observed). This is in consistent with approximately a 30 % overlap of the beams in the experiment. The imperfect overlap is due to phase-matching requirements, introducing an angle of ~0.1 radians between the pump beam and the generated photons, with the pump beam size of ~0.9 mm and a lamellae distance of 5 mm. Despite this overlap deficiency, which reduces the intensity variation visibility, the efficient background noise elimination by coincidence and photon energy discrimination allows precise measurements of very small phase variations with the present method.

DISCUSSION

We demonstrate x-ray quantum nonlinear interferometry, using SPDC of x-ray pump photons to generate correlated idler and signal photon pairs. In our setup, dispersion-induced phase shifts accumulated by the three modes as they traverse a phase object are converted into intensity variations at the interferometer's output, enabling precise determination of phase shifts. We have leveraged the inherent pairing of photons in the SPDC process to demonstrate that coincidence and energy conservation filtering of these correlated photons allow for highly sensitive phase measurements, even in environments with substantial noise. This powerful noise discrimination, made possible by our ability to identify photon pairs within a very noisy environment despite the very weak gain of the SPDC sources, is a uniquely quantum phenomenon with no classical analog, as demonstrated in several experiments in the optical range (*41*, *42*).

Although our focus was on time and energy correlations, other degrees of freedom, such as position or momentum (k-vector) correlations, could further enhance the SNR. The use of fast pixelated detectors, such as Medipix3 (*43*–*45*), could facilitate this advancement. The main practical limitations of the scheme presented here are the time and energy resolutions of the coincidence measurement system. Notably, a recent experiment has demonstrated improved performance with enhanced electronics (*46*), suggesting that the SNR could be improved by approximately a factor of 10 compared to our current results. Further improvements will likely require advancements in detector technology. Last, we note that phase measurements using intensity correlations with classical synchrotron radiation at x-ray wavelengths have been demonstrated (*47*). However, quantum correlations of the type used here are anticipated to provide even stronger results.

Our scheme enables the measurement of phase information even within optically opaque materials, expanding the scope and applicability of SU(1,1) interferometry to previously unexplored domains. For x-rays, this type of interferometer is very appealing since it eliminates the need for an analyzer crystal to detect subwavelength spatial shifts in the interference pattern. Furthermore, since the phase variation in an SU(1,1) interferometer is imprinted in the phase matching variation rather than in spatial variation, the interferometer is expected to be more stable against mechanical vibrations (*22*). By eliminating the need for stringent stability requirements hampering the performance of conventional x-ray interferometers, our method unleashes the potential of x-ray quantum interferometry, promising unparalleled sensitivity in quantum metrology. Consequently, we foresee our work laying foundations for the implementation of x-ray crystal interferometry with separate crystals, overcoming a major limitation in this field. Extending our work to phase contrast imaging with a pixelated detector is straightforward and holds promise for highly sensitive imaging methods. This is because phase contrast often surpasses transmission contrast in many samples. The potential of this approach has already been demonstrated in the visible range (*39*, *40*).

MATERIALS AND METHODS

Materials—Interferometer and phase object

Figure 5 shows our interferometer and a typical phase object. Figure 5A is a photograph of the interferometer, with details of its fabrication described in (*37*, *38*). It is a monolithic device cut from a perfect silicon single crystal, with lamellas ~0.25 mm thick, 12 mm high, 25 mm wide, and spaced 5 mm apart. The x-ray absorption by each lamella is ~0.02% for the 35-keV pump and around 0.2% for the signal and idler modes. The (1,1,1) reflection plane is normal to the lamellas, as shown in Fig. 5B. The silicon membranes (Fig. 5C) were obtained from Norcada Inc. in three thicknesses as described in Table 1. By stacking these membranes in various

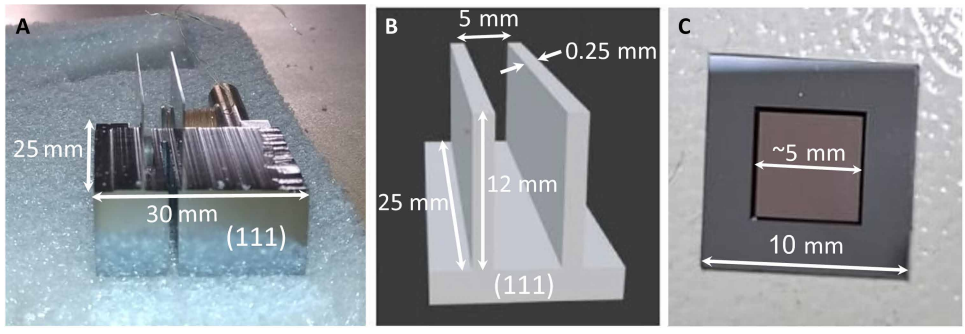

Fig. 5. Interferometer and membrane. (**A** and **B**) The interferometer and (**C**) a typical membrane phase object

Table 1. Dimensions of the membranes used, in combination, as a phase object.

Model	Frame size (mm)	Frame thickness (μm)	Membrane thickness (μm)	Membrane dimensions (mm)
SM10480N	10 × 10 (±0.2)	300 (±10)	2 (±0.5)	4.8 × 4.8 (±0.05)
SM10500P	10 × 10 (±0.2)	300 (±10)	10 (±0.5)	5 × 5 (±0.05)
SM10500Q	10 × 10 (±0.2)	300 (±10)	20 (±0.5)	5 × 5 (±0.05)

combinations, phase objects of thicknesses ranging from 2 to 28 μm were obtained. This approach allowed precise control over the beam's phase modulation.

Methods

Introductory measurements were carried out at the Nano/Micro Diffraction Imaging beamline (ID01) at the European synchrotron radiation facility (ESRF) (*48*). The results shown in Figs. 3 and 4 were obtained at the RIKEN SR physics beamline (BL19LXU) of the SPring-8 facility (*49*). We used a Si(111) monochromator to narrow the bandwidth of the input beam to ~1 eV. The spot size of the pump beam was defined by slits of 0.9 mm by 0.3 mm (horizontal by vertical). To avoid detector count-rate saturation, the input flux was reduced by an aluminium absorber. The output photons, of energies centered at 17.5 keV, were measured by two energy-resolving photon-counting Amptek XR-100SDD Silicon Drift Detectors (SDDs). The detectors were connected to a PicoScope 6407 high-speed digitizer for data analysis. The time and energy intervals are determined by the system resolution. The coincidence time window of the detectors was 1000 ns. For the energy conservation discrimination, the tolerance on the photon energies was ±3 keV.

Supplementary Materials

This PDF file includes:

Supplementary Text
Figs. S1 and S2
References

REFERENCES AND NOTES

1. U. Bonse, M. Hart, An x-ray interferometer. *Appl. Phys. Lett.* **6**, 155–156 (1965).
2. P. Becker, P. De Bièvre, K. Fujii, M. Glaeser, B. Inglis, H. Luebbig, G. Mana, Considerations on future redefinitions of the kilogram, the mole and of other units. *Metrologia* **44**, 1 (2007).
3. P. Becker, Tracing the definition of the kilogram to the Avogadro constant using a silicon single crystal. *Metrologia* **40**, 366 (2003).
4. G. Basile, A. Bergamin, G. Cavagnero, G. Mana, E. Vittone, G. Zosi, Measurement of the silicon (220) lattice spacing. *Phys. Rev. Lett.* **72**, 3133 (1994).
5. L. Ferroglio, G. Mana, E. Massa, Si lattice parameter measurement by centimeter x-ray interferometry. *Opt. Express* **16**, 16877–16888 (2008).
6. T. J. Davis, D. Gao, T. E. Gureyev, A. W. Stevenson, S. W. Wilkins, Phase-contrast imaging of weakly absorbing materials using hard x-rays. *Nature* **373**, 595–598 (1995).
7. F. Pfeiffer, T. Weitkamp, O. Bunk, C. David, Phase retrieval and differential phase-contrast imaging with low-brilliance x-ray sources. *Nat. Phys.* **2**, 258–261 (2006).
8. A. Momose, T. Takeda, Y. Itai, K. Hirako, Phase-contrast x-ray computed tomography for observing biological soft tissues. *Nat. Med.* **2**, 473–475 (1996).
9. H. Miao, A. Panna, A. A. Gomella, E. E. Bennett, S. Znati, L. Chen, H. Wen, A universal moiré effect and application in x-ray phase-contrast imaging. *Nat. Phys.* **12**, 830–834 (2016).
10. A. Yoneyama, D. Takamatsu, T. T. Lwin, S. Yamada, T. Takakuwa, K. Hyodo, K. Hirano, S. Takeya, Crystal-based x-ray interferometry and its application to phase-contrast x-ray imaging, Zeff imaging, and x-ray thermography. *Appl. Sci.* **13**, 5424 (2023).
11. P. Diemoz, A. Bravin, M. Langer, P. Coan, Analytical and experimental determination of signal-to-noise ratio and figure of merit in three phase-contrast imaging techniques. *Opt. Express* **20**, 27670–27690 (2012).
12. P. Modregger, B. R. Pinzer, T. Thüring, S. Rutishauser, C. David, M. Stampanoni, Sensitivity of x-ray grating interferometry. *Opt. Express* **19**, 18324–18338 (2011).
13. F. Pfeiffer, M. Bech, O. Bunk, P. Kraft, E. F. Eikenberry, C. Brönnimann, C. Grünzweig, C. David, Hard-x-ray dark-field imaging using a grating interferometer. *Nat. Mater.* **7**, 134–137 (2008).
14. M. O. Scully, K. Drühl, Quantum eraser: A proposed photon correlation experiment concerning observation and "delayed choice" in quantum mechanics. *Phys. Rev. A* **25**, 2208–2213 (1982).
15. B. Yurke, S. L. McCall, J. R. Klauder, SU(2) and SU(1,1) interferometers. *Phys. Rev. A* **33**, 4033 (1986).
16. J. Jing, C. Liu, Z. Zhou, Z. Y. Ou, W. Zhang, Realization of a nonlinear interferometer with parametric amplifiers. *Appl. Phys. Lett.* **99**, 011110 (2011).
17. R. N. Shakhmuratov, F. Vagizov, O. Kocharovskaya, Single gamma-photon revival from sandwich absorbers. *Phys. Rev. A* **87**, 013807 (2013).
18. P. Helistö, I. Tittonen, M. Lippmaa, T. Katila, Gamma echo. *Phys. Rev. Lett.* **66**, 2037–2040 (1991).
19. D. Watts, J. Bordes, J. Brown, A. Cherlin, R. Newton, J. Allison, M. Bashkanov, N. Efthimiou, N. Zachariou, Photon quantum entanglement in the mev regime and its application in pet imaging. *Nat. Commun.* **12**, 2646 (2021).
20. A. Schori, D. Borodin, K. Tamasaku, S. Shwartz, Ghost imaging with paired x-ray photons. *Phys. Rev. A* **97**, 063804 (2018).
21. S. Sofer, E. Strizhevsky, A. Schori, K. Tamasaku, S. Shwartz, Quantum enhanced x-ray detection. *Phys. Rev. X* **9**, 031033 (2019).

22. M. V. Chekhova, Z. Y. Ou, Nonlinear interferometers in quantum optics. *Adv. Opt. Photonics* **8**, 104–155 (2016).
23. Y. Shaked, Y. Michael, R. Z. Vered, L. Bello, M. Rosenbluh, A. Pe'er, Lifting the bandwidth limit of optical homodyne measurement with broadband parametric amplification. *Nat. Commun.* **9**, 609 (2018).
24. Y. Michael, I. Jonas, L. Bello, M. E. Meller, E. Cohen, M. Rosenbluh, A. Pe'er, Augmenting the sensing performance of entangled photon pairs through asymmetry. *Phys. Rev. Lett.* **127**, 173603 (2021).
25. M. Manceau, G. Leuchs, F. Khalili, M. Chekhova, Detection loss tolerant supersensitive phase measurement with an SU(1,1) interferometer. *Phys. Rev. Lett.* **119**, 223604 (2017).
26. G. Frascella, S. Agne, F. Y. Khalili, M. V. Chekhova, Overcoming detection loss and noise in squeezing-based optical sensing. *npj Quantum Inform* **7**, 72 (2021).
27. S. Meir, Y. Tamir, H. Duadi, E. Cohen, M. Fridman, Ultrafast temporal SU(1,1) interferometer. *Phys. Rev. Lett.* **130**, 253601 (2023).
28. M. Manceau, K. Y. Spasibko, G. Leuchs, R. Filip, M. V. Chekhova, Indefinite-mean pareto photon distribution from amplified quantum noise. *Phys. Rev. Lett.* **123**, 123606 (2019).
29. M. Manceau, F. Khalili, M. Chekhova, Improving the phase super-sensitivity of squeezing-assisted interferometers by squeeze factor unbalancing. *New J. Phys.* **19**, 013014 (2017).
30. Y. Michael, L. Bello, M. Rosenbluh, A. Pe'er, Squeezing-enhanced Raman spectroscopy. *npj Quantum Inf* **5**, 81 (2019).
31. A. Eldan, O. Gilon, A. Lagemi, E. F. Furman, A. Pe'er, Multiplexed processing of quantum information across an ultra-wide optical bandwidth. arXiv:2310.17819 [quant-ph] (2023).
32. E. Strizhevsky, D. Borodin, A. Schori, S. Francoual, R. Röhlsberger, S. Shwartz, Efficient interaction of heralded x-ray photons with a beam splitter. *Phys. Rev. Lett.* **127**, 013603 (2021).
33. P. Eisenberger, S. L. McCall, X-ray parametric conversion. *Phys. Rev. Lett.* **26**, 684–688 (1971).
34. S. Shwartz, R. N. Coffee, J. M. Feldkamp, Y. Feng, J. B. Hastings, G. Y. Yin, S. E. Harris, X-ray parametric down-conversion in the Langevin regime. *Phys. Rev. Lett.* **109**, 013602 (2012).
35. S. Shwartz, S. E. Harris, Polarization entangled photons at x-ray energies. *Phys. Rev. Lett.* **106**, 080501 (2011).
36. I. Freund, B. F. Levine, Parametric conversion of x rays. *Phys. Rev. Lett.* **23**, 854–857 (1969).
37. M. Deutsch, M. Hart, Electronic charge distribution in silicon. *Phys. Rev. B* **31**, 3846 (1985).
38. M. Deutsch, M. Hart, A new approach to the measurement of x-ray structure amplitudes determined by the Pendellösung method. *Acta Crystallogr. A* **41**, 48–55 (1985).
39. J. Szuniewicz, S. Kurdziałek, S. Kundu, W. Zwolinski, R. Chrapkiewicz, M. Lahiri, R. Lapkiewicz, Noise-resistant phase imaging with intensity correlation. *Sci. Adv.* **9**, eadh5396 (2023).
40. G. Thekkadath, D. England, F. Bouchard, Y. Zhang, M. Kim, B. Sussman, Intensity interferometry for holography with quantum and classical light. *Sci. Adv.* **9**, eadh1439 (2023).
41. R. Z. Vered, Y. Shaked, Y. Ben-Or, M. Rosenbluh, A. Pe'Er, Classical-to-quantum transition with broadband four-wave mixing. *Phys. Rev. Lett.* **114**, 063902 (2015).
42. N. Nechushtan, H. Zhang, M. Meller, A. Pe'er, Optimal detection of ultra-broadband bi-photons with quantum nonlinear SU(1,1) interference. *New J. Phys.* **23**, 113003 (2021).
43. R. Ballabriga, M. Campbell, E. Heijne, X. Llopart, L. Tlustos, W. Wong, Medipix3: A 64 k pixel detector readout chip working in single photon counting mode with improved spectrometric performance. *Nucl. Instrum. Methods Phys. Res., Sect. A* **633**, S15–S18 (2011).
44. V. Sriskaran, J. Alozy, R. Ballabriga, M. Campbell, P. Christodoulou, E. Heijne, A. Koukab, T. Kugathasan, X. Llopart, M. Piller, A. Pulli, J. M. Sallese, L. Tlustos, High-rate, high-resolution single photon x-ray imaging: Medipix4, a large 4-side buttable pixel readout chip with high granularity and spectroscopic capabilities. *J. Instrum.* **19**, P02024 (2024).
45. J. C. Goodrich, R. Mahon, J. Hanrahan, M. Dziubelski, R. A. Abrahao, S. Karmakar, K. J. Gofron, T. Caswell, D. Allan, L. Berman, A. Fluerasu, A. Nomerotski, C. DaVià, S. McSweeney, Imaging of x-ray pairs in a spontaneous parametric down-conversion process. arXiv:2310.13078 [physics.optics] (2023).
46. N. J. Hartley, D. Hodge, T. Buckway, R. Camacho, P. Chow, E. Christie, A. Gleason, S. Glenzer, A. Halavanau, A. M. Hardy, C. Recker, S. Sheehan, S. Shwartz, H. Tarvin, M. Ware, J. Wunschel, Y. Xiao, R. L. Sandberg, G. Walker, Confirming x-ray parametric down conversion by time-energy correlation. *Results Phys* **57**, 107328 (2024).
47. K. Tamasaku, T. Ishikawa, M. Yabashi, T. Ishikawa, X-ray interferometry with multicrystal components using intensity correlation. *Phys. Rev. Lett.* **88**, 044801 (2002).
48. S. J. Leake, V. Favre-Nicolin, E. Zatterin, M. I. Richard, S. Fernandez, G. Chahine, T. Zhou, P. Boesecke, H. Djazouli, T. U. Schülli, Coherent nanoscale x-ray probe for crystal interrogation at ID01, ESRF - The European Synchrotron. *Mater. Des.* **119**, 470–471 (2017).
49. M. Yabashi, T. Mochizuki, H. Yamazaki, S. Goto, H. Ohashi, K. Takeshita, T. Ohata, T. Matsushita, K. Tamasaku, Y. Tanaka, T. Ishikawa, Design of a beamline for the SPring-8 long undulator source 1. *Nucl. Instrum. Methods Phys. Res., Sect. A* **467**, 678–681 (2001).
50. V. Balic, D. A. Braje, P. Kolchin, G. Y. Yin, S. E. Harris, Generation of paired photons with controllable waveforms. *Phys. Rev. Lett.* **94**, 183601 (2005).
51. P. Kolchin, Electromagnetically-induced-transparency-based paired photon generation. *Phys. Rev. A* **75**, 033814 (2007).
52. C. H. Raymond Ooi, Continuous source of phase-controlled entangled two-photon laser. *Phys. Rev. A* **76**, 013809 (2007).
53. C. H. Raymond Ooi, M. O. Scully, Q. Sun, M. S. Zubairy, Correlation of photon pairs from the double Raman amplifier: Generalized analytical quantum Langevin theory. *Phys. Rev. A* **75**, 013820 (2007).
54. S. Du, J. Wen, M. H. Rubin, Narrowband biphoton generation near atomic resonance. *J. Opt. Soc. Am. B* **25**, C98–C108 (2008).

Acknowledgments: We thank the SPring-8 facility for granting beamtime on beamline BL19LXU. We thank the ESRF for granting beamtime on beamline ID01. We thank S. E. Harris for sharing his notes. This study is dedicated to M. Hart CBE FRS and the late U. Bonse on the 60th anniversary of their invention of the crystal x-ray interferometer (*1*). **Funding:** This work is supported by the Israel Science Foundation (ISF) (847/21); Y.K. and E.K. acknowledge the support of Canada Research Chair and Quantum Sensors Challenge Program at the National Research Council of Canada. E.C. acknowledge the support of the European Union's Horizon Europe research and innovation program under grant agreement no. 101178170 and the Israel Science Foundation (ISF) (2208/24). **Author contributions:** Conceptualization: Y.K., S.S., E.C., and A.P. Investigation: Y.K., E.S., H.A., M.D., K.T., and T.S. Resources: M.D., K.T., and T.S. Supervision: S.S. and E.K. Validation: M.D., E.C., A.P., and E.K. Writing—original draft: Y.K. and S.S. Writing—review and editing: M.D., E.C., A.P., E.K., and S.S. **Competing interests:** The authors declare that they have no competing interests. **Data and materials availability:** All data needed to evaluate the conclusions in the paper are present in the paper and/or the Supplementary Materials.

Submitted 12 February 2025
Accepted 25 July 2025
Published 27 August 2025
10.1126/sciadv.adw3893